



MOX-Report No. 97/2024

**Designing novel vascular stents with enhanced mechanical behavior  
through topology optimization of existing devices**

Ferro, N.; Mezzadri, F.; Carbonaro, D.; Galligani, E.; Gallo, D.; Morbiducci,  
U.; Chiastra, C.; Perotto, S.

MOX, Dipartimento di Matematica  
Politecnico di Milano, Via Bonardi 9 - 20133 Milano (Italy)

[mox-dmat@polimi.it](mailto:mox-dmat@polimi.it)

<https://mox.polimi.it>

# Designing novel vascular stents with enhanced mechanical behavior through topology optimization of existing devices

Nicola Ferro<sup>1</sup>, Francesco Mezzadri<sup>2</sup>, Dario Carbonaro<sup>3</sup>,  
Emanuele Galligani<sup>2</sup>, Diego Gallo<sup>3</sup>, Umberto Morbiducci<sup>3</sup>,  
Claudio Chiastra<sup>3</sup>, Simona Perotto<sup>1</sup>

November 12, 2024

<sup>1</sup> MOX – Department of Mathematics  
Politecnico di Milano  
Piazza L. da Vinci, 32, I-20133 Milano, Italy

<sup>2</sup> Department of Engineering “Enzo Ferrari”  
University of Modena and Reggio Emilia,  
Via P. Vivarelli, 10/1, I-41125 Modena, Italy

<sup>3</sup> Polito<sup>BIO</sup>MED Lab  
Department of Mechanical and Aerospace Engineering  
Politecnico di Torino,  
Viale Duca degli Abruzzi, 24, I-10129 Torino, Italy

## Abstract

A variety of different vascular stent designs are currently available on the market, featuring different geometries, manufacturing materials, and physical characteristics. Here, we propose a framework for designing innovative stents that replicate and enhance the mechanical properties of existing devices. The framework includes a SIMP-based topology optimization formulation, assisted by the homogenization theory to constrain the mechanical response, along with a minimum length scale requirement to ensure manufacturability to the designed devices. The optimization problem, discretized on a sequence of computational meshes anisotropically adapted, generates a 2D stent unit cell, which can be automatically converted into a 3D digital version of the device. This virtual prototype is validated through *in silico* testing via a radial crimping simulation to assess the stent insertion into the catheter, prior to implantation. The results prove that the proposed framework can identify stent designs that are competitive with respect to existing devices in terms of relevant clinical requirements, such as foreshortening, radial stiffness and surface contact area.

**Keywords:** Stent design; Topology optimization; Homogenization; Finite elements; Anisotropic adapted mesh; Virtual prototyping.

# 1 Introduction

Vascular stents are minimally invasive medical devices commonly used to treat diseased blood vessels. These cylindrical hollow structures are first crimped to a reduced diameter and then deployed inside blood vessels at the site of vascular obstruction to provide structural support to the vessel wall and prevent lumen narrowing. A variety of stent designs are currently available on the market, featuring different shapes, sizes and materials, depending on the specific pathology and implantation site. Stents can be divided into two main categories: balloon-expandable and self-expandable devices. Self-expandable stents, typically made of super-elastic nickel-titanium (NiTi), are manufactured slightly larger than the vessel diameter and elastically return to their original shape after being crimped and released from a catheter. In contrast, balloon-expandable stents, usually made of stainless-steel, cobalt or platinum chromium alloy, are manufactured in a crimped state and expanded to the vessel wall using balloon inflation. To facilitate delivery and placement, both balloon- and self-expandable stents are designed with a narrow profile in their compressed (i.e., crimped) state [1, 2, 3, 4].

The alternating arrangement of material and void areas in stent geometry has been proven to influence the biomechanical behavior of the device [3, 4, 5, 6, 7, 8, 9], affecting factors such as the contact area between the device and vessel wall, radial stiffness, foreshortening, and blood flow disturbances, which can potentially impact clinical outcomes. Specifically, the contact area and the blood flow alterations are associated with the onset of post-interventional adverse events, such as in-stent restenosis and stent thrombosis [10, 11]. Radial stiffness reflects the stent capability of scaffolding the vessel without damage [12, 13, 3], while foreshortening affects how accurately the device covers the full length of a vascular lesion during implantation [12, 13, 3]. As a result, analyzing the mechanical properties of a stent provides insights into the safety and successful outcome of the stenting procedure. In this regard, computational methods, particularly *in silico* models, have emerged as powerful tools for virtually characterizing and optimizing stent design, and are becoming increasingly important in the medical device industry by supporting the design process [14, 15, 16, 17, 18, 19, 20, 21, 22, 23, 24, 25, 26, 27].

Among the most prominent computational methods for the optimal design of structures that optimally respond to external stimuli, topology optimization (TO) has gained massive momentum [28]. In this context, TO has proved effective in designing innovative stents with optimized mechanical and fluid dynamics performance. For example, the identification of optimal designs of vascular stents has been approached using the TO module of commercial software [29], as well as through a nonlinear elasticity-guided TO approach [30]. Similarly, TO has been applied to the design of auxetic self-expandable stents [31, 32]. More recently, a TO-based design and verifi-

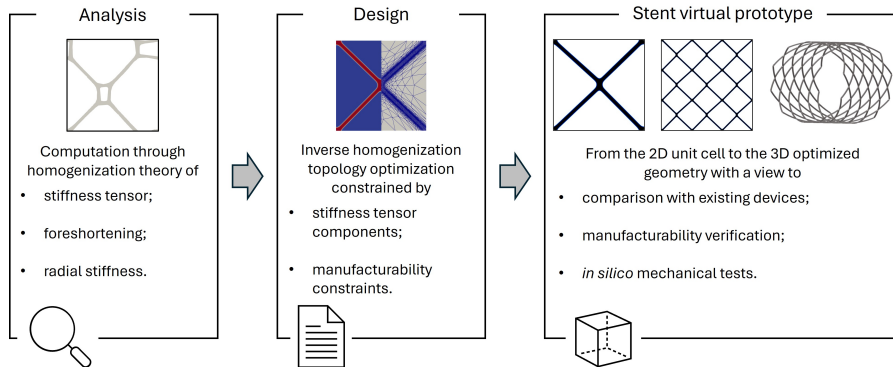


Figure 1: Pipeline of the proposed method: starting from the analysis of an existing stent unit cell (left panel), an inverse homogenization topology optimization is settled (center panel) with a view to the generation of a stent virtual prototype (right panel).

cation pipeline has been proposed in [33], while, in [34], the Cosserat theory has been used for optimizing a polymeric stent.

Unlike these contributions, where the optimization process focuses on designing new stents from scratch, the present study proposes an Analyze-To-Optimize inverse homogenization TO problem in a finite element framework, enriched by an anisotropic mesh adaptation procedure. Specifically, we characterize existing self-expandable stents in terms of the associated mechanical properties. Subsequently, we reproduce and/or enhance such features by generating innovative devices starting from the design of the associated unit cells, which are also suited to a manufacturing phase. This framework follows a digital twinning approach [35], with the ultimate goal of providing a virtual prototype of a newly designed device that can be used for inspection and for *in silico* tests with a view to further characterization and validation.

The paper is structured as follows. In Sect. 2, we present the mathematical tools to characterize an existing self-expandable stent and formulate a TO framework to design innovative manufacturable devices using an Analyze-To-Optimize approach. In Sect. 3, we focus on the numerical discretization of the optimization problem, which proves to provide stent unit cells that are either consistent or innovative when compared with existing unit cell layouts. In Sect. 4, we detail how to generate the 3D devices starting from the optimized planar unit cells by discussing the geometric and mechanical properties of the stent geometries with a view to virtual prototyping. Finally, in the last section, we conclude by outlining potential future directions for the design of innovative stents.

## 2 Mathematical formulation for stent design

We propose a computational pipeline, as illustrated in Fig. 1, which begins with the analysis of an existing stent design and concludes with the generation of a new device with competitive mechanical properties. In this section, we firstly present the mathematical models necessary to characterize stents in terms of the corresponding homogenized stiffness tensor, foreshortening, and radial stiffness (left panel). Subsequently, we formulate an optimization problem aimed at designing stent geometries that replicate (and possibly improve) the observed mechanical properties (center panel). The 3D virtual prototype generation and the associated testing (right panel) will be addressed in Sect. 3.

### 2.1 Stent analysis

A generic vascular stent can be conceptualized as a periodic repetition of a single unit cell along the radial and axial directions of a hollow cylinder (Fig. 2, left). By assuming that the stent thickness is negligible with respect to the axial and radial dimensions, it is possible to characterize the mechanical performance of the whole stent by analyzing the planar unit cell alone, in accordance with homogenization theory [33, 36].

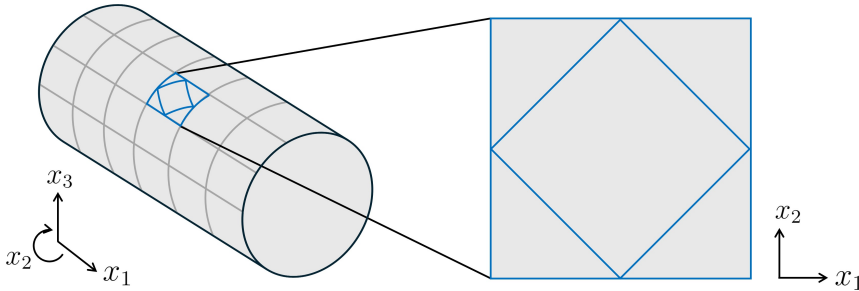


Figure 2: Schematic representation of the generic vascular stent (left) and of the planar unit cell (right).

#### 2.1.1 Direct homogenization

In order to provide a characterization of the stent from the mechanical viewpoint, we resort to the homogenization theory. In general, we denote by  $\Omega$  the macroscopic domain in  $\mathbb{R}^2$ , with coordinates  $(x_1, x_2)$ , obtained by the periodic repetition of the unit cell  $Y \subset \mathbb{R}^2$ , consisting of a specific material/void layout. The repetition period  $\delta$  is assumed to be small compared to the size of  $\Omega$ . As reference physical model, we adopt the linear elasticity setting, such that the static equilibrium of  $\Omega$  is governed by the partial

differential equation (PDE)

$$-\nabla \cdot \boldsymbol{\sigma}(\mathbf{u}) = \mathbf{b}, \quad (1)$$

where  $\mathbf{u} = (u_1, u_2)^T : \Omega \rightarrow \mathbb{R}^2$  is the vector of the displacement;

$$\boldsymbol{\sigma}(\mathbf{u}) = E\boldsymbol{\varepsilon}(\mathbf{u}) = \frac{1}{2}E[\nabla\mathbf{u} + (\nabla\mathbf{u})^T] \quad (2)$$

denotes the stress field, with

$$\boldsymbol{\sigma} = \begin{pmatrix} \sigma_{11} \\ \sigma_{22} \\ \sigma_{12} \end{pmatrix}, \quad \boldsymbol{\varepsilon}(\mathbf{u}) = \begin{pmatrix} \varepsilon_{11} \\ \varepsilon_{22} \\ 2\varepsilon_{12} \end{pmatrix}, \quad E = \begin{pmatrix} E_{1111} & E_{1122} & E_{1112} \\ E_{2211} & E_{2222} & E_{2212} \\ E_{1211} & E_{1222} & E_{1212} \end{pmatrix} \quad (3)$$

the stress, strain vectors and the stiffness tensor in Voigt notation, respectively;  $\mathbf{b}$  models the body forces, here selected as the null vector. In particular, the stiffness tensor depends on the properties of the selected material. For instance, in case of an isotropic medium,  $E$  can be defined in terms of the Young's modulus,  $\Xi$ , and the Poisson's ratio,  $\nu$ , of the material, being

$$E = \begin{pmatrix} \lambda + 2\mu & \lambda & 0 \\ \lambda & \lambda + 2\mu & 0 \\ 0 & 0 & \mu \end{pmatrix}, \quad (4)$$

with  $\lambda = \Xi\nu/[(1+\nu)(1-2\nu)]$ , and  $\mu = \Xi/[2(1+\nu)]$  the material Lamè coefficients. We observe that the stiffness tensor depends on the spatial coordinates due to the void/solid alternation in the unit cell and to the  $\delta$ -periodicity of  $Y$ . To address this complexity, the theory of homogenization considers a multiscale approach through an asymptotic analysis for  $\delta$  approaching 0 [37, 38]. Thus, the microscopic heterogeneities become increasingly negligible and the properties of the macroscopic structure are characterized by the homogenized stiffness tensor,  $E^H$ , whose components are given by

$$E_{ijkl}^H(\mathbf{u}^{*,ij}, \mathbf{u}^{*,kl}) = \frac{1}{|Y|} \int_Y [\boldsymbol{\sigma}(\mathbf{u}^{0,ij}) - \boldsymbol{\sigma}(\mathbf{u}^{*,ij})] : [\boldsymbol{\varepsilon}(\mathbf{u}^{0,kl}) - \boldsymbol{\varepsilon}(\mathbf{u}^{*,kl})] dY, \quad (5)$$

where  $:$  denotes the standard tensorial inner product,  $\mathbf{u}^{*,mn}$ , with  $mn = ij, kl \in \{11, 22, 12\}$ , denotes the microscopic mechanical response to the independent test displacements  $\mathbf{u}^{0,11} = (x_1, 0)^T$ ,  $\mathbf{u}^{0,22} = (0, x_2)^T$ , and  $\mathbf{u}^{0,12} = (x_2, 0)^T$ . In particular,  $\mathbf{u}^{*,mn}$  coincides with the solution to the variational problem: for  $mn \in \{11, 22, 12\}$ , find  $\mathbf{u}^{*,mn} \in V_P$ , such that

$$\int_Y \boldsymbol{\sigma}(\mathbf{u}^{*,mn}) : \boldsymbol{\varepsilon}(\mathbf{v}) dY = \int_Y \boldsymbol{\sigma}(\mathbf{u}^{0,mn}) : \boldsymbol{\varepsilon}(\mathbf{v}) dY \quad \forall \mathbf{v} \in V_P, \quad (6)$$

where  $V_P$  is the periodic Sobolev space  $[H_P^1(Y)]^2$  of the vector-valued functions in  $H^1(Y)$  satisfying periodic conditions on the boundary  $\partial Y$  (we refer to [39] for all the details).

### 2.1.2 Stent foreshortening and radial stiffness evaluation

Although the homogenized tensor  $E^H$  can be employed to characterize the macroscopic properties of the vascular stent, it is not straightforward to link the tensor components to mechanical properties of clinical interest. Here, we are interested in analyzing the stent response under radial compression to establish the relationships between  $E^H$  and the foreshortening  $f$  (i.e., the length reduction during deployment), to evaluate the correct placement of the deployed device within the vessel, as well as between  $E^H$  and the radial stiffness  $K_r$  (i.e., the resistance to radial force), which is responsible for the scaffolding function of the stent. To this aim, we consider the typical stent geometry characterized by thickness  $t$ , radius  $r_0$ , length at rest  $l_0$ , where  $t$  is assumed to be small with respect to  $r_0$  and  $l_0$ . These hypotheses, combined with the typical radial loading scenario, lead us to consider the stent in a plane stress state. We adopt a cylindrical coordinate system as illustrated in Figure 2, left panel. Furthermore, we assume  $E^H$  to be orthotropic, as the stent is supposed to be uniformly compressed in the radial direction during the crimping phase. Hence, the homogenized variant of the stress-strain relation (3) simplifies to

$$\begin{pmatrix} \sigma_{11} \\ \sigma_{22} \\ \sigma_{12} \end{pmatrix} = \begin{pmatrix} E_{1111}^H & E_{1122}^H & 0 \\ E_{2211}^H & E_{2222}^H & 0 \\ 0 & 0 & E_{1212}^H \end{pmatrix} \begin{pmatrix} \varepsilon_{11} \\ \varepsilon_{22} \\ 2\varepsilon_{12} \end{pmatrix}. \quad (7)$$

For an infinitesimal strain, we introduce the compatibility equations [40]

$$\begin{cases} \varepsilon_{11} = \frac{\partial u_1}{\partial x_1} \\ \varepsilon_{22} = \frac{1}{x_3} \frac{\partial u_2}{\partial x_2} + \frac{u_3}{x_3} \\ 2\varepsilon_{12} = \frac{\partial u_1}{\partial x_2} + \frac{\partial u_2}{\partial x_1}, \end{cases} \quad (8)$$

where  $u_3$  denotes the radial displacement and  $x_3$  the radial coordinate. If the axial symmetry is maintained, the above system of equations simplifies to

$$\begin{cases} \varepsilon_{11} = \frac{\partial u_1}{\partial x_1} \\ \varepsilon_{22} = \frac{u_3}{x_3} \\ 2\varepsilon_{12} = \frac{\partial u_2}{\partial x_1}. \end{cases}$$

As loading scenario, we prescribe a constant radial displacement,  $u_3^*$ , which changes the initial length  $l_0$  into the final value  $l$ , so that

$$\varepsilon_{11} = \frac{l - l_0}{l_0}, \quad \varepsilon_{22} = \frac{u_3^*}{r_0}, \quad \sigma_{11} = 0. \quad (9)$$

From (7) and (9)<sub>3</sub>, it follows

$$\sigma_{11} = E_{1111}^H \varepsilon_{11} + E_{1122}^H \varepsilon_{22} = 0, \quad (10)$$

which leads to

$$\varepsilon_{11} = -\frac{E_{1122}^H}{E_{1111}^H} \varepsilon_{22}. \quad (11)$$

This equation, together with (9)<sub>1,2</sub>, provides the following measure of the foreshortening as a function of the components of  $E^H$ , being

$$f := \frac{l - l_0}{l_0} = \frac{E_{1122}^H}{E_{1111}^H} \frac{u_3^*}{r_0} = f^m \frac{u_3^*}{r_0}, \quad (12)$$

where  $f^m = E_{1122}^H/E_{1111}^H$  coincides with the microscopic foreshortening due to the unit cell geometry.

We can proceed similarly for the radial stiffness. Starting from the definition of radial force  $F_3 = 2\pi F_2$ , where  $F_2 = \sigma_{22} l_0 t$  is the hoop force [41, 42], and thanks to (7), we have

$$\sigma_{22} = E_{2211}^H \varepsilon_{11} + E_{2222}^H \varepsilon_{22},$$

which, together with (9)<sub>2</sub>, (11), and the definition of  $F_2$ , leads to

$$K_r := \frac{F_3}{u_3^*} = \frac{2\pi l_0 t}{r_0} \left( E_{2222}^H - \frac{(E_{1122}^H)^2}{E_{1111}^H} \right) = \frac{2\pi l_0 t}{r_0} K_r^m, \quad (13)$$

with  $K_r^m = E_{2222}^H - (E_{1122}^H)^2/E_{1111}^H$  the microscopic radial stiffness due to the unit cell geometry. For a more detailed derivation and analysis, we refer to [36].

## 2.2 Stent unit cell design via topology optimization

With reference to the second panel of Fig. 1, we present an efficient method to design unit cells that constitute innovative stents characterized by specific engineering properties. The main goal of this approach is to analyze an existing unit cell stent design,  $Y_{\text{obs}}$ , to retrieve its mechanical features using relations (12)-(13), and to provide alternative unit cells with similar or enhanced mechanical properties.

To this end, we employ a topology optimization (TO) framework. TO enables the distribution of material inside a domain  $D \subset \mathbb{R}^d$ , with  $d = 2, 3$ , by modifying the associated topology (i.e., creating, moving or deleting the structural boundaries), provided that certain constraints on the optimization procedure are satisfied [43]. Several mathematical methods can be adopted to address a TO problem, mainly diversified for the mathematical

tool used to track the material/void interface. Level set and density-based approaches are majorly used for the mathematical rigor and ease of implementation [44, 45]. In this study, we adopt a density-based TO approach, which can be generally expressed as

$$\min_{\rho \in S} J(\mathbf{w}_1(\rho), \dots, \mathbf{w}_N(\rho); \rho) : \begin{cases} a_{i,\rho}(\mathbf{w}_i(\rho), \mathbf{v}) = f_{i,\rho}(\mathbf{v}) \quad \forall \mathbf{v} \in V \\ \underline{c}_j \leq c_j(\mathbf{w}_1(\rho), \dots, \mathbf{w}_N(\rho); \rho) \leq \bar{c}_j \\ \underline{\rho} \leq \rho \leq 1, \end{cases} \quad (14)$$

with  $i = 1, \dots, N$ , and  $j = 1, \dots, M$ , where  $\rho$  is the density variable that describes the material/void distribution, being  $\rho \simeq 1$  in the regions occupied by full material and  $\rho \simeq \underline{\rho}$  for the areas of void, with  $\underline{\rho} \ll 1$  a positive value that guarantees the well-posedness of formulation (14), and  $S = H^1(D; [\underline{\rho}, 1])^1$ ; functions  $\mathbf{w}_i(\rho)$  are the state variables belonging to a suitable function space  $V$ , for  $i = 1, \dots, N$ ;  $J(\cdot; \rho)$  is the objective functional that drives the optimization, possibly depending on the state variables and on the density. As for the constraints in (14), the first  $N$  relations are the state equations in weak form that models the physics underlying the minimization process, with  $a_{i,\rho}(\cdot, \cdot)$  and  $f_{i,\rho}(\cdot)$  the bilinear and linear forms, respectively, and  $\mathbf{v}$  the test function in  $V$ ; the inequality constraints introduce a lower and an upper control through values  $\underline{c}_j$  and  $\bar{c}_j$ , respectively, on the design and/or physical quantities of interest  $c_j(\cdot, \rho)$ , with  $j = 1, \dots, M$ ; finally, the last box constraint imposes the admissible range for  $\rho$ .

The dependency of the forms  $a_{i,\rho}(\cdot, \cdot)$  and  $f_{i,\rho}(\cdot)$  on the density variable  $\rho$  may vary with the chosen TO model. In this study, we consider the Solid Isotropic Material with Penalization (SIMP) approach, where standard material Lamé coefficients are modified by a power law penalization, namely multiplied by  $\rho^p$ , with  $p > 0$  the penalization exponent [45]. This modeling has the objective to suppress intermediate density values, thus favoring a final quasi-binary configuration, with  $\rho \simeq 1$  or  $\rho \simeq \underline{\rho}$  almost everywhere, for a sharp definition of the structure topology.

### 2.2.1 Inverse homogenization TO to control structural properties

The density-based TO formulation (14) is now framed in an inverse homogenization setting in order to design engineered stent unit cells. In detail, we consider the 2D unit cell geometry as the design domain, namely  $D = Y \subset \mathbb{R}^2$ . Moreover, with reference to [10, 11] where the contact area between the stent and the vessel is identified as a risk factor for tissue ingrowth, in-stent restenosis and thrombosis, we choose to drive the TO problem by

---

<sup>1</sup>A priori,  $S$  could coincide with the space  $L^\infty(D; [\underline{\rho}, 1])$ . We opt for a higher regular space with a view to the optimization discrete setting.

minimizing the volume fraction in  $Y$  occupied by the full material, i.e.,

$$J(\rho) = \mathcal{M} = \frac{1}{|Y|} \int_Y \rho dY, \quad (15)$$

with  $\rho \in S_P = H_P^1(Y)$ . Concerning the state variables in (14), following [45, 38, 46], we set  $\mathbf{w}_1(\rho) = \mathbf{u}^{*,11}$ ,  $\mathbf{w}_2(\rho) = \mathbf{u}^{*,22}$ , and  $\mathbf{w}_3(\rho) = \mathbf{u}^{*,12}$ , solutions to the problems: for  $ij \in \{11, 22, 12\}$ , find  $\mathbf{u}^{*,ij} \in V_P$  such that

$$\int_Y \rho^p \boldsymbol{\sigma}(\mathbf{u}^{*,ij}) : \boldsymbol{\varepsilon}(\mathbf{v}) dY = \int_Y \rho^p \boldsymbol{\sigma}(\mathbf{u}^{0,ij}) : \boldsymbol{\varepsilon}(\mathbf{v}) dY \quad \forall \mathbf{v} \in V_P, \quad (16)$$

which correspond to the SIMP-modified version of (6) and identify the bilinear and linear forms in (14). Here, we drop the dependence of  $\mathbf{u}^{*,ij}$  on the density  $\rho$  to simplify the notation.

In order to achieve prescribed homogenized properties of interest, we control the values of the 6 homogenized stiffness components, by identifying the constrained quantities in (14) with

$$\begin{aligned} c_1(\mathbf{u}^{*,11}, \mathbf{u}^{*,11}; \rho) &= E_{1111,\rho}^H(\mathbf{u}^{*,11}, \mathbf{u}^{*,11}), \\ c_2(\mathbf{u}^{*,22}, \mathbf{u}^{*,22}; \rho) &= E_{2222,\rho}^H(\mathbf{u}^{*,22}, \mathbf{u}^{*,22}), \\ c_3(\mathbf{u}^{*,12}, \mathbf{u}^{*,12}; \rho) &= E_{1212,\rho}^H(\mathbf{u}^{*,12}, \mathbf{u}^{*,12}), \\ c_4(\mathbf{u}^{*,11}, \mathbf{u}^{*,22}; \rho) &= E_{1122,\rho}^H(\mathbf{u}^{*,11}, \mathbf{u}^{*,22}), \\ c_5(\mathbf{u}^{*,11}, \mathbf{u}^{*,12}; \rho) &= E_{1112,\rho}^H(\mathbf{u}^{*,11}, \mathbf{u}^{*,12}), \\ c_6(\mathbf{u}^{*,22}, \mathbf{u}^{*,12}; \rho) &= E_{2212,\rho}^H(\mathbf{u}^{*,22}, \mathbf{u}^{*,12}), \end{aligned}$$

where the components  $E_{ijkl,\rho}^H$ , for  $ij, kl$  in  $\{11, 22, 12\}$ , are the density-weighted versions of (5), given by

$$E_{ijkl,\rho}^H(\mathbf{u}^{*,ij}, \mathbf{u}^{*,kl}) = \frac{1}{|Y|} \int_Y \rho^p [\boldsymbol{\sigma}(\mathbf{u}^{0,ij}) - \boldsymbol{\sigma}(\mathbf{u}^{*,ij})] : [\boldsymbol{\varepsilon}(\mathbf{u}^{0,kl}) - \boldsymbol{\varepsilon}(\mathbf{u}^{*,kl})] dY. \quad (17)$$

The associated lower and upper bounds are selected as

$$\begin{aligned} c_1 &= (1 - \gamma) E_{1111,\text{obs}}^H & \bar{c}_1 &= (1 + \gamma) E_{1111,\text{obs}}^H, \\ c_2 &= (1 - \gamma) E_{2222,\text{obs}}^H & \bar{c}_2 &= (1 + \gamma) E_{2222,\text{obs}}^H, \\ c_3 &= (1 - \gamma) E_{1212,\text{obs}}^H & \bar{c}_3 &= (1 + \gamma) E_{1212,\text{obs}}^H, \\ c_4 &= (1 - \gamma) E_{1122,\text{obs}}^H & \bar{c}_4 &= (1 + \gamma) E_{1122,\text{obs}}^H, \\ c_5 &= -E_{\min} & \bar{c}_5 &= E_{\min}, \\ c_6 &= -E_{\min} & \bar{c}_6 &= E_{\min}, \end{aligned}$$

where  $E_{ijkl,\text{obs}}^H$  is the generic stiffness tensor component computed by (5) when associated with design  $Y = Y_{\text{obs}}$ ,  $\gamma \in [0, 1]$  tunes the width of the admissible range of variation for the constraints, and  $E_{\min} > 0$  is a constant sufficiently small used to enforce the homogenized tensor to be orthotropic.

### 2.2.2 A length scale control for manufacturability

The minimization of the functional in (15) a priori would lead towards the erosion of the layout. However, designs characterized by thin stent struts are unfeasible from the point of view of the physical manufacturing of the device. Indeed, stent manufacturing traditionally resorts to laser-cutting technologies that cannot deliver devices whose strut size is below a certain threshold. Therefore, a manufacturing constraint must be imposed to control the strut length scale. This requirement is recurrent and consolidated in the literature [47, 48].

Here, we adopt the formulation in [48], where the density  $\rho$  is substituted by the physical field  $\tilde{\rho}$  obtained by filtering procedures. First, we solve the smoothing Helmholtz-type differential equation

$$\begin{cases} -r_H^2 \Delta \tilde{\rho} + \tilde{\rho} = \rho & \text{in } Y \\ \frac{\partial \tilde{\rho}}{\partial n} = 0 & \text{on } \partial Y, \end{cases} \quad (18)$$

where  $r_H$  is related to the threshold for the minimum strut size,  $S_{\min,2D}$ , through the relation  $S_{\min,2D} = 4\sqrt{3} r_H$  [49].

Subsequently, the smoothed density  $\tilde{\rho}$  is mapped into a (quasi) black-and-white configuration by the Heaviside-like transformation

$$\tilde{\bar{\rho}} = \begin{cases} \frac{1}{2} [e^{-\beta(1-2\tilde{\rho})} - (1-2\tilde{\rho})e^{-\beta}] & \text{if } 0 \leq \tilde{\rho} \leq \frac{1}{2} \\ \frac{1}{2} [1 - e^{-\beta(2\tilde{\rho}-1)} - (1-2\tilde{\rho})e^{-\beta}] + \frac{1}{2} & \text{if } \frac{1}{2} \leq \tilde{\rho} \leq 1, \end{cases} \quad (19)$$

where  $\beta > 0$  tunes the steepness of the filtering, regulating the severity of the transition from 0 to 1 across the intermediate densities.

Thus, the TO formulation in (14) is particularized to the Analyze-To-Optimize for Manufacturable Stents (ATOMS) formulation, which reads as:

$$\min_{\rho \in S_P} \mathcal{M}(\bar{\rho}) : \left\{ \begin{array}{l}
\int_{\Omega} \bar{\rho}^p \boldsymbol{\sigma}(\mathbf{u}^{*,11}) : \boldsymbol{\varepsilon}(\mathbf{v}) d\Omega, = \int_{\Omega} \bar{\rho}^p \boldsymbol{\sigma}(\mathbf{u}^{0,11}) : \boldsymbol{\varepsilon}(\mathbf{v}) d\Omega \quad \forall \mathbf{v} \in V_P \\
\int_{\Omega} \bar{\rho}^p \boldsymbol{\sigma}(\mathbf{u}^{*,22}) : \boldsymbol{\varepsilon}(\mathbf{v}) d\Omega, = \int_{\Omega} \bar{\rho}^p \boldsymbol{\sigma}(\mathbf{u}^{0,22}) : \boldsymbol{\varepsilon}(\mathbf{v}) d\Omega \quad \forall \mathbf{v} \in V_P \\
\int_{\Omega} \bar{\rho}^p \boldsymbol{\sigma}(\mathbf{u}^{*,12}) : \boldsymbol{\varepsilon}(\mathbf{v}) d\Omega, = \int_{\Omega} \bar{\rho}^p \boldsymbol{\sigma}(\mathbf{u}^{0,12}) : \boldsymbol{\varepsilon}(\mathbf{v}) d\Omega \quad \forall \mathbf{v} \in V_P \\
(1 - \gamma) E_{1111, \text{obs}}^H \leq E_{1111, \bar{\rho}}^H(\mathbf{u}^{*,11}, \mathbf{u}^{*,11}) \leq (1 + \gamma) E_{1111, \text{obs}}^H \\
(1 - \gamma) E_{2222, \text{obs}}^H \leq E_{2222, \bar{\rho}}^H(\mathbf{u}^{*,22}, \mathbf{u}^{*,22}) \leq (1 + \gamma) E_{2222, \text{obs}}^H \\
(1 - \gamma) E_{1212, \text{obs}}^H \leq E_{1212, \bar{\rho}}^H(\mathbf{u}^{*,12}, \mathbf{u}^{*,12}) \leq (1 + \gamma) E_{1212, \text{obs}}^H \\
(1 - \gamma) E_{1122, \text{obs}}^H \leq E_{1122, \bar{\rho}}^H(\mathbf{u}^{*,11}, \mathbf{u}^{*,22}) \leq (1 + \gamma) E_{1122, \text{obs}}^H \\
-E_{\min} \leq E_{1112, \bar{\rho}}^H(\mathbf{u}^{*,11}, \mathbf{u}^{*,12}) \leq E_{\min} \\
-E_{\min} \leq E_{2212, \bar{\rho}}^H(\mathbf{u}^{*,22}, \mathbf{u}^{*,12}) \leq E_{\min} \\
\rho \leq \bar{\rho} \leq 1,
\end{array} \right. \quad (20)$$

with  $\mathcal{M}(\bar{\rho})$  as in (15) and  $\bar{\rho}$  defined through (18) and (19). ATOMS formulation will be instrumental to the proposal of new stent designs.

### 3 ATOMS to replicate and enhance existing unit cells performance

In this section, we detail the numerical setting used to provide the discrete counterpart of (20). This formulation, along with the stent property characterization in Sect. 2.1.2, allows us to reproduce as well as to upgrade the performance of existing stent unit cells.

#### 3.1 A customized discretization for ATOMS

Generic TO settings like (14) are typically discretized and solved by resorting to diverse numerical optimization methods. For instance, it is common to approximate the state equations and variables, and the density function in a finite element (FE) setting, and then to employ iterative large-scale optimizers, such as the Methods of Moving Asymptotes (MMA) [50] or the Interior Point OPTimizer (IPOPT) [51]. The choice of the computational mesh associated with the FE discretization plays a crucial role in the optimization process [52, 45]. In particular, a too coarse grid can result in designs with poor boundary quality, requiring invasive post-processing, while a too re-

finer mesh increases computational costs. To address these challenges, the authors in [53] introduce the SIMPATY algorithm for the SIMP-based TO of structures. SIMPATY alternates the optimizer iterations with an anisotropic mesh adaptation procedure, thus generating highly refined designs at an affordable computational effort. As an improvement of the basic algorithm, in [54, 55], SIMPATY is enriched with a control on the mesh anisotropy to crowd elongated elements in correspondence of the material boundary, while resorting to isotropic triangles inside the structure. Stretched elements allow sharply resolving the boundary layers at the material/void interface, while equilateral triangles avoid to bias the FE mechanical analysis [56]. In the context of the design of engineered metamaterials, a combination of SIMPATY with inverse homogenization is formalized into the microSIMPATY algorithm. MicroSIMPATY has proved to inherit the high accuracy and reliability properties of SIMPATY, thus justifying the successful application to diverse multi-objective and multi-physics frameworks [46, 57, 58, 59, 33] and to ATOMS formulation.

To this aim, we define the mesh,  $\mathcal{T}_h = \{K\}$ , that tessellates the domain through triangles, we introduce the discrete spaces

$$S_P^h = V_h^1 \cap S_P, \quad V_P^h = [V_h^1]^2 \cap V_P,$$

and the associated discrete density, state, and test functions

$$\bar{\rho}_h \in S_P^h, \quad \mathbf{u}_h^{*,ij}, \mathbf{v}_h \in V_P^h,$$

respectively, for  $ij = \{11, 22, 12\}$ , where

$$V_h^1 = \{v_h \in C^0(\bar{Y}) : v_h|_K \in \mathbb{P}_1(K) \forall K \in \mathcal{T}_h\}$$

is the continuous affine FE space, with  $\mathbb{P}_1(K)$  the space of polynomials of degree 1 in  $K$ .

The minimization process in (20) is carried out through an iterative loop consisting of two main phases.

As a first step, we compute the discrete solutions,  $\mathbf{u}_h^{*,ij}$ , to the state equations on  $\mathcal{T}_h$ . These quantities are provided as an input to an optimizer together with the objective functional,  $\mathcal{M}$ , the two-sided constraints and the associated derivatives with respect to  $\rho$ , to yield the optimized physical density.

In the second phase of ATOMS, the optimized  $\bar{\rho}_h$  is used to update the computational mesh into a new grid suited to track the material/void interface of the current layout, with a view to the next optimization step. For this purpose, we follow [60], where the authors drive an anisotropic mesh adaptation procedure through the generalization of the Zienkiewicz-Zhu error estimator [61, 62] to an anisotropic environment. The estimator controls the  $H^1$ -seminorm of the discretization error associated with a target quantity, here identified with the density  $\bar{\rho}$ . Specifically, the global anisotropic

error estimator for the seminorm  $|\bar{\rho} - \bar{\rho}_h|_{H^1(Y)}$  is defined by

$$\eta^2 = \sum_{K \in \mathcal{T}_h} \eta_K^2,$$

with

$$\eta_K^2 = \frac{1}{\lambda_{1,K} \lambda_{2,K}} \sum_{i=1}^2 \lambda_{i,K}^2 (\mathbf{r}_{i,K}^T \mathbf{G}_{\Delta_K}(\mathcal{E}(\bar{\rho}_h)) \mathbf{r}_{i,K}), \quad (21)$$

the elementwise error estimator. In particular, according to the anisotropic setting in [63, 60], quantities  $\lambda_{i,K}$  and  $\mathbf{r}_{i,K}$  coincide with the length and the direction of the semi-axes of the ellipse circumscribed to the generic element  $K$ , with  $i = 1, 2$  and  $\lambda_{1,K} \geq \lambda_{2,K} > 0$ , and do characterize the size (through lengths  $\lambda_{i,K}$ ), the shape (through the aspect ratio  $s_K = \lambda_{1,K}/\lambda_{2,K} \geq 1$ ) and the orientation (through directions  $\mathbf{r}_{i,K}$ ) of  $K$ ;  $\mathcal{E}(\bar{\rho}_h) = \mathbf{R}(\bar{\rho}_h) - \nabla \bar{\rho}_h$  is the recovered error that surrogates  $\nabla \bar{\rho} - \nabla \bar{\rho}_h$ , with

$$\mathbf{R}(\bar{\rho}_h)(\mathbf{x}) = |\Delta_K|^{-1} \sum_{T \in \Delta_K} |T| \nabla \bar{\rho}_h|_T(\mathbf{x}) \quad \mathbf{x} \in K,$$

the so-called recovered gradient and  $\Delta_K = \{T \in \mathcal{T}_h : T \cap K \neq \emptyset\}$  the patch of elements associated with  $K$ ;  $\mathbf{G}_{\Delta_K}(\mathcal{E}(\bar{\rho}_h))$  is the symmetric positive semidefinite matrix, with components

$$[\mathbf{G}_{\Delta_K}(\mathcal{E}(\bar{\rho}_h))]_{ij} = \sum_{T \in \Delta_K} \int_T (\mathcal{E}(\bar{\rho}_h))_i (\mathcal{E}(\bar{\rho}_h))_j dT \quad i, j = 1, 2,$$

and  $(\mathcal{E}(\bar{\rho}_h))_k$  the  $k$ -th component of the recovered error, for  $k = 1, 2$ .

Different strategies are available in the reference literature to commute  $\eta$  into practical information to generate the new adapted mesh. We adopt the metric-based approach in [64], where the new grid is built in order to ensure a certain accuracy,  $\mathbf{tol}_\eta$ , on the error  $|\bar{\rho} - \bar{\rho}_h|_{H^1(Y)}$ , while minimizing the mesh cardinality,  $\#\mathcal{T}_h$ , and equidistributing the error throughout the adapted grid. As derived in [64], the lengths,  $\lambda_{i,K}^A$ , and the directions,  $\mathbf{r}_{i,K}^A$ , identifying the new adapted mesh are given by

$$\begin{aligned} \lambda_{1,K}^A &= g_{2,K}^{-1/2} \left( \frac{\mathbf{tol}_\eta^2}{2\#\mathcal{T}_h C_K} \right)^{1/2}, & \mathbf{r}_{1,K}^A &= \mathbf{g}_{2,K}, \\ \lambda_{2,K}^A &= g_{1,K}^{-1/2} \left( \frac{\mathbf{tol}_\eta^2}{2\#\mathcal{T}_h C_K} \right)^{1/2}, & \mathbf{r}_{2,K}^A &= \mathbf{g}_{1,K}, \end{aligned} \quad (22)$$

with  $C_K$  a computable constant and where  $\{g_{i,K}, \mathbf{g}_{i,K}\}_{i=1}^2$  are the eigenpairs associated with matrix  $\mathbf{G}_{\Delta_K}(\mathcal{E}(\bar{\rho}_h))/|\Delta_K|$ .

Successively, the spacing in (22) is preserved only near the material/void

boundary, while a uniform isotropic tessellation of size  $h_{\text{iso}}$  is used to discretize the material portion of the design domain. As numerically proved in [55, 54, 33], this hybrid meshing strategy guarantees a sharp description of the layout and the reliability of the mechanical analysis.

Algorithm 1 formalizes the two phases of ATOMS procedure. The **while**

---

**Algorithm 1** ATOMS

---

- 1: **Input:**  $\text{tol}_J, \text{tol}_\eta, \text{tol}_M, \mathbf{k}_{\max}, \bar{\rho}_h^{(0)}, \mathcal{T}_h^{(0)}, p, \rho, \gamma, E_{1111, \text{obs}}^H, E_{2222, \text{obs}}^H, E_{1212, \text{obs}}^H, E_{1122, \text{obs}}^H, E_{\min}, r_H, \beta, h_{\text{iso}}$
  - 2: Set  $\mathbf{k} = 0, \text{err}_M = 1 + \text{tol}_M$ ;
  - 3: **while**  $\text{err}_M > \text{tol}_M$  and  $\mathbf{k} < \mathbf{k}_{\max}$  **do**
  - 4:  $\bar{\rho}_h^{(\mathbf{k}+1)} = \text{Optimize}(\bar{\rho}_h^{(\mathbf{k})}, \mathcal{T}_h^{(\mathbf{k})}, p, \mathcal{Q}, \nabla_\rho \mathcal{Q}, \dots$
  - 5:  $\rho, \gamma, E_{1111, \text{obs}}^H, E_{2222, \text{obs}}^H, E_{1212, \text{obs}}^H, E_{1122, \text{obs}}^H, E_{\min}, \dots$
  - 6:  $r_H, \beta, \text{tol}_J$ );
  - 7:  $\mathcal{T}_h^{(\mathbf{k}+1)} = \text{AdaptMesh}(\bar{\rho}_h^{(\mathbf{k}+1)}, \mathcal{T}_h^{(\mathbf{k})}, \text{tol}_\eta, h_{\text{iso}})$ ;
  - 8:  $\bar{\rho}_h^{(\mathbf{k}+1)} = \text{Project}(\mathcal{T}_h^{(\mathbf{k}+1)}, \mathcal{T}_h^{(\mathbf{k})}, \bar{\rho}_h^{(\mathbf{k}+1)})$ ;
  - 9:  $\text{err}_M = |\#\mathcal{T}_h^{(\mathbf{k}+1)} - \#\mathcal{T}_h^{(\mathbf{k})}| / \#\mathcal{T}_h^{(\mathbf{k})}$ ;
  - 10:  $\mathbf{k} = \mathbf{k} + 1$ ;
  - 11: **end while**
  - 12:  $\tau = \bar{\rho}_h^{(\mathbf{k})}$ ;
  - 13:  $E_\tau^H = \text{Homogenize}(\tau)$ ;
  - 14: **Output:**  $\tau, E_\tau^H$
- 

loop alternates between the two phases described above until a maximum number,  $\mathbf{k}_{\max}$ , of iterations is reached or the mesh cardinality stagnates. During the optimization, starting from the current configuration  $(\bar{\rho}_h^{(\mathbf{k})}$  and  $\mathcal{T}_h^{(\mathbf{k})}$ ), routine **Optimize** in lines 4-6 is fed with all the data involved by the minimization in (20), namely, the SIMP penalization exponent; the objective functional and the constrained quantities, cumulatively indicated by

$$\mathcal{Q} = (\mathcal{M}, E_{1111, \bar{\rho}}^H, E_{2222, \bar{\rho}}^H, E_{1212, \bar{\rho}}^H, E_{1122, \bar{\rho}}^H, E_{1112, \bar{\rho}}^H, E_{2212, \bar{\rho}}^H)$$

and the associated derivative with respect to  $\rho, \nabla_\rho \mathcal{Q}$  (we refer to [65], where a Lagrangian approach is employed to compute such a quantity); the data required to define the two-sided inequalities; the parameters tuning the filtering procedures; the tolerance,  $\text{tol}_J$ , used for the stopping criterion to

halt the routine.

Successively, the mesh adaptation procedure is performed to deliver the hybrid domain tessellation, merging anisotropic mesh adaptation with a uniform isotropic discretization. This task is accomplished in line 7 through routine `AdaptMesh` whose inputs are the optimized physical density,  $\bar{\rho}_h^{(k+1)}$ , with the associated mesh, along with the tolerance,  $\text{tol}_\eta$ , and the size,  $h_{\text{iso}}$ , for the isotropic tessellation guiding the generation of the adapted mesh. Lines 8-9 are pivotal to the next iteration, by projecting the optimized density onto the new adapted mesh and evaluating the relative variation in mesh cardinality with a view to the stagnation stopping criterion.

The algorithm ultimately delivers the optimized physical density,  $\tau = \bar{\rho}_h^{(k)}$ , and the corresponding homogenized stiffness tensor,  $E_\tau^H$ , computed through routine `Homogenize` in line 13 that implements (17) for  $\rho = \tau$ .

In the numerical assessment of Sect. 3.2, Algorithm 1 is implemented in a FreeFEM-based in-house code. In particular, the `Optimize` routine coincides with the IPOPT large scale optimizer [51], while the `AdaptMesh` module takes advantage of the built-in mesh generator, available in the platform [66].

### 3.2 Design and comparative analysis of optimized stent unit cells

In this section, we utilize Algorithm 1 to design innovative stent unit cells, starting from three layouts in Fig. 3, named  $Y_{\text{obs}}^{\text{D1}}$ ,  $Y_{\text{obs}}^{\text{D2}}$ ,  $Y_{\text{obs}}^{\text{EVFX}}$ . These unit cells are inspired by existing designs. In particular,  $Y_{\text{obs}}^{\text{D1}}$  and  $Y_{\text{obs}}^{\text{D2}}$  are the geometries validated in [33], where the struts are slightly inflated to account for a minimum length scale. Unit cell  $Y_{\text{obs}}^{\text{EVFX}}$  is inspired by the Everflex stent (EV3, Medtronic, Dublin, Ireland). If we manufacture the three layouts in Fig. 3 with an isotropic material characterized by  $\Xi = 60$  and  $\nu = 0.33$ , the corresponding homogenized stiffness tensor, contact area, microscopic radial stiffness and foreshortening are<sup>2</sup>

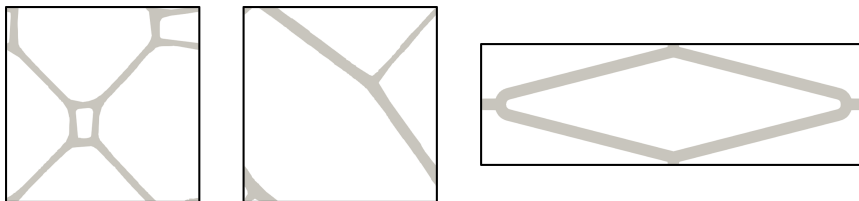


Figure 3: Stent unit cells  $Y_{\text{obs}}^{\text{D1}}$ ,  $Y_{\text{obs}}^{\text{D2}}$ ,  $Y_{\text{obs}}^{\text{EVFX}}$  (left-right).

<sup>2</sup>In the design phase, following [33], we consider adimensional quantities. We assign consistent units of measure in Sect. 4 to embed the virtual prototypes in real-world scenarios.

$$\begin{aligned}
E_{Y_{\text{obs}}^{\text{D1}}}^H &= \begin{pmatrix} 2.547 & 2.566 & 0.071 \\ 2.566 & 2.745 & 0.075 \\ 0.071 & 0.075 & 0.514 \end{pmatrix}, & \mathcal{M}_{Y_{\text{obs}}^{\text{D1}}} &= 0.163, \\
& & K_r^m &= 0.161, \quad f^m = 1.000, \\
E_{Y_{\text{obs}}^{\text{D2}}}^H &= \begin{pmatrix} 1.888 & 1.912 & -1.366 \\ 1.912 & 2.015 & -1.403 \\ -1.366 & -1.403 & 1.048 \end{pmatrix}, & \mathcal{M}_{Y_{\text{obs}}^{\text{D2}}} &= 0.132, \\
& & K_r^m &= 0.078, \quad f^m = 1.010, \\
E_{Y_{\text{obs}}^{\text{EVFX}}}^H &= \begin{pmatrix} 9.317 & 0.750 & 0.000 \\ 0.750 & 0.065 & 0.000 \\ 0.000 & 0.000 & 0.536 \end{pmatrix}, & \mathcal{M}_{Y_{\text{obs}}^{\text{EVFX}}} &= 0.190, \\
& & K_r^m &= 0.005, \quad f^m = 0.080.
\end{aligned} \tag{23}$$

We remark that  $Y_{\text{obs}}^{\text{D1}}$  features similar stiffness components along the  $x_1$ - and  $x_2$ -directions and a quasi-orthotropic behavior. Layout  $Y_{\text{obs}}^{\text{D2}}$  exhibits comparable stiffness values along the Cartesian direction, but lacks orthotropicity. Design  $Y_{\text{obs}}^{\text{EVFX}}$  is characterized by a marked difference in components  $E_{1111}^H$  and  $E_{2222}^H$ , the latter being smaller by two orders of magnitude. Concerning  $K_r^m$  and  $f^m$ , it is possible to observe that the first two designs are characterized by high microscopic foreshortening and moderate microscopic radial stiffness, while the Everflex-inspired design shows negligible microscopic foreshortening and small microscopic radial stiffness. Finally, all the contact areas are below 20%, so that the considered stents are lightweight.

For the three unit cell designs, we aim to reproduce the homogenized stiffness tensor components in (23), except for the ones responsible for orthotropicity, (consistency test) and to enhance a mechanical property of interest –  $f^m$  or  $K_r^m$  – with respect to the reference values in (23) (enhancement test). To this aim, we resort to ATOMS algorithm, by setting

$$\begin{aligned}
\text{tol}_J &= 5e - 16, \text{tol}_\eta = 1e - 4, \text{tol}_M = 5e - 3, \mathbf{k}_{\max} = 30, \bar{\rho}_h^{(0)} = 0.3, \\
p &= 4, \rho = 1e - 4, E_{\min} = 1e - 3, r_H = 8 \cdot 20 / [88(4\sqrt{3})], h_{\text{iso}} = 10/150,
\end{aligned}$$

as input parameters for all the test cases, while we specify the initial mesh and the upper and lower bounds for the constrained components for each run. Moreover, we increase  $\beta$  from 1 to 20 throughout the optimizer iterations. We observe that the value selected for  $r_H$  and the range of variation adopted for  $\beta$  allow to guarantee a realistic minimum length scale of the stent struts  $S_{\min,2D} = 20/88$ , up to a safety factor here set to 8 (see Sect. 4).

### 3.3 Design $\tau_{\text{D1}}$

For the first numerical assessment, domain  $Y$  is chosen as a  $10 \times 10$  square, initially discretized through a triangular structured tessellation,  $\mathcal{T}_h^{(0)}$ , comprising 11250 elements. The values for  $E_{1111,\text{obs}}^H$ ,  $E_{2222,\text{obs}}^H$ ,  $E_{1212,\text{obs}}^H$ ,  $E_{1122,\text{obs}}^H$  coincide with those in the first row of (23) associated with  $Y_{\text{obs}}^{\text{D1}}$ .

**Consistency test** By setting  $\gamma = 0.15$ , we obtain the topology,  $\tau_{D1}$ , in Fig. 4 (top row, left panel) after 26 iterations. The associated homogenized stiffness tensor, the contact area, the microscopic radial stiffness and foreshortening are

$$E_{\tau_{D1}}^H = \begin{pmatrix} 2.195 & 2.175 & -0.003 \\ 2.175 & 2.330 & -0.003 \\ -0.003 & -0.003 & 0.517 \end{pmatrix}, \quad \mathcal{M}_{\tau_{D1}} = 0.157, \quad K_r^m = 0.174, \quad f^m = 0.990. \quad (24)$$

The obtained values for the stiffness tensor components align with the cor-

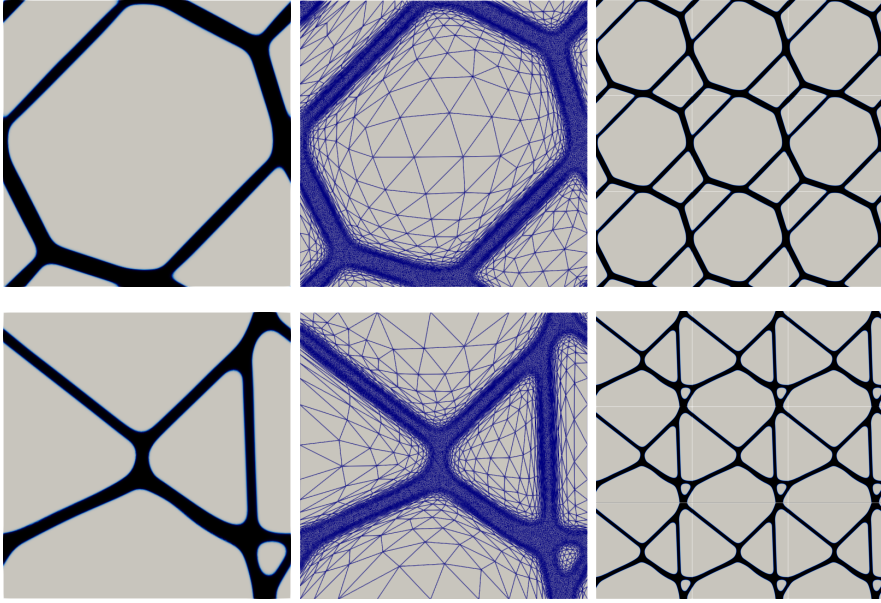


Figure 4: Design  $\tau_{D1}$ : consistency (top) and enhancement (bottom) test results in terms of optimized unit cell (left), adapted computational mesh (center), and  $3 \times 3$  planar periodic pattern (right).

responding values in (23). Consequently, foreshortening and radial stiffness are comparable to those of  $Y_{\text{obs}}^{D1}$ , exhibiting a negligible decrement and increment for  $f^m$  and  $K_r^m$ , respectively. On the contrary, the mass fraction of  $\tau_{D1}$  (and, thus, the contact area) is reduced when compared with  $Y_{\text{obs}}^{D1}$  mass. This outcome is highly relevant for clinical applications, suggesting that there is room for improvement in the devices currently in use by exploiting ATOMS formulation.

The corresponding adapted mesh is presented in the top row, center panel of Fig. 4. This tessellation features 14660 triangles, with a maximum stretching factor equal to  $s_K^{\text{max}} = 364.60$ . Such large element elongation is particularly evident along the structure boundary. Conversely, small isotropic triangles can be observed inside the structure, according to the isotropic size imposed

through  $h_{\text{iso}}$ . This fine tessellation is responsible for the accurate approximate values in (24).

Finally, the periodic repetition of  $\tau_{\text{D1}}$  on the plane yields the pattern in the right panel of the top row.

**Enhancement test** For the enhancement of the analyzed design  $Y_{\text{obs}}^{\text{D1}}$ , we aim to reduce the microscopic foreshortening. With this goal, with reference to (12), we change the constraint for  $E_{1122, \bar{\rho}}^H$  in (20) into

$$(1 - 3\gamma)E_{1122, \text{obs}}^H \leq E_{1122, \bar{\rho}}^H(\mathbf{u}^{*,11}, \mathbf{u}^{*,22}) \leq E_{1122, \text{obs}}^H,$$

pushing the component towards a lower value, keeping  $\gamma = 0.15$ ,

The optimized layout, named  $\tau_{\text{D1,E}}$ , is obtained in 25 iterations and is shown in Fig. 4 (bottom row, left panel). The new topology is characterized by the following quantitative results

$$E_{\tau_{\text{D1,E}}}^H = \begin{pmatrix} 2.156 & 1.475 & 0.000 \\ 1.475 & 2.325 & -0.001 \\ 0.000 & -0.001 & 0.431 \end{pmatrix}, \quad \mathcal{M}_{\tau_{\text{D1,E}}} = 0.146, \\ K_r^m = 1.316, \quad f^m = 0.680.$$

The stiffness tensor components are consistent with the bounds imposed in the design constraints. Compared to  $Y_{\text{obs}}^{\text{D1}}$ , the unit cell yielded by Algorithm 1 is characterized by a smaller contact area and a 32% reduction in foreshortening, at the expense of an increased radial stiffness due to the smaller value for  $(E_{1122}^H)^2/E_{1111}^H$  in (13) (from a geometrical viewpoint, the presence of the vertical strut in  $\tau_{\text{D1,E}}$  is likely responsible for the higher radial stiffness).

The adapted mesh in the bottom row, center panel of Fig. 4, consists of 14326 elements and presents a major triangle elongation near the boundary of the struts, with  $s_K^{\text{max}} = 489.68$ .

### 3.4 Design $\tau_{\text{D2}}$

Analogously as in the previous test case, domain  $Y$  in (20) is chosen as a  $10 \times 10$  square, consistent with the aspect ratio of the unit cell  $Y_{\text{obs}}^{\text{D2}}$ . This domain is tessellated with the mesh  $\mathcal{T}_h^{(0)}$  in Section 3.4. The values for  $E_{1111, \text{obs}}^H$ ,  $E_{2222, \text{obs}}^H$ ,  $E_{1212, \text{obs}}^H$ ,  $E_{1122, \text{obs}}^H$  are reported in the second row of (23) corresponding to  $Y_{\text{obs}}^{\text{D2}}$ .

**Consistency test** The consistency run is performed by selecting  $\gamma = 0.15$ . The execution ends in 29 iterations, resulting in the unit cell displayed in Fig. 5 (top row, left panel). The obtained topology,  $\tau_{\text{D2}}$ , is relatively simple and exhibits an asymmetric geometry. The output mechanical properties

are

$$E_{\tau_{D2}}^H = \begin{pmatrix} 1.600 & 1.633 & 0.000 \\ 1.633 & 1.709 & 0.001 \\ 0.000 & 0.001 & 0.929 \end{pmatrix}, \quad \mathcal{M}_{\tau_{D2}} = 0.120, \\ K_r^m = 0.0423, \quad f^m = 1.020.$$

Cross-comparing the stiffness tensor component values with the correspond-

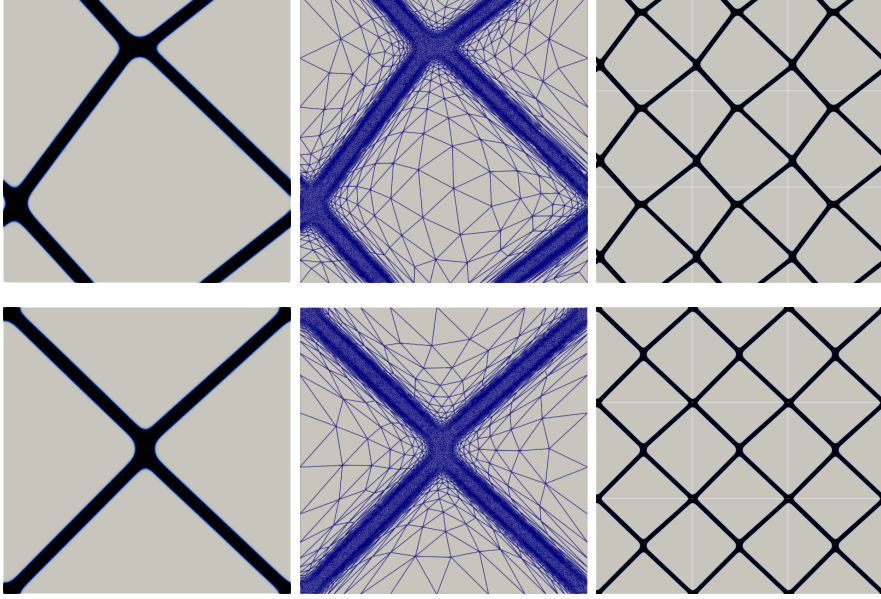


Figure 5: Design  $\tau_{D2}$ : consistency (top) and enhancement (bottom) test results in terms of optimized unit cell (left), adapted computational mesh (center), and  $3 \times 3$  planar periodic pattern (right).

ing ones in  $E_{Y_{\text{obs}}^H}^H$ , we observe that all the constrained quantities are compliant with the imposed bounds. Moreover, the imposition of orthotropy guarantees that the resulting layout has vanishing components  $E_{1112, \tau_{D2}}^H$  and  $E_{2212, \tau_{D2}}^H$ , thus overcoming the anomalous behavior observed in  $E_{Y_{\text{obs}}^H}^H$ .

As far as  $f^m$  and  $K_r^m$  are concerned, we can notice that  $\tau_{D2}$  is consistent with  $Y_{\text{obs}}^{D2}$  in terms of foreshortening up to a 1% mismatch. Vice versa, the radial stiffness characterizing  $\tau_{D2}$  is lower than the one in the original design due to the nonlinear relation among the stiffness tensor components in (13).

The computational mesh that assists the design phase is shown in the top row, center panel of Fig. 5. This anisotropic grid is composed of 11906 elements and is characterized by isotropic triangles inside the unit cell topology and by stretched elements aligned with the structure struts. Due to the marked directionality of the straight diagonal components, the mesh elements reach a value of 985.73 for the maximum aspect ratio  $s_K^{\text{max}}$ . In the right panel, we show the  $3 \times 3$  periodic repetition of  $\tau_{D2}$ , which highlights the asymmetry of the layout.

**Enhancement test** We exploit the ATOMS framework to design a stent unit cell that guarantees the mechanical properties of  $Y_{\text{obs}}^{\text{D2}}$ , except for the radial stiffness that we aim to reduce. For this purpose, after setting  $\gamma = 0.15$ , we modify the second two-sided inequality in (20) with

$$(1 - 3\gamma)E_{2222,\text{obs}}^H \leq E_{2222,\bar{\rho}}^H(\mathbf{u}^{*,22}, \mathbf{u}^{*,22}) \leq E_{2222,\text{obs}}^H$$

to favor low values for  $E_{2222,\bar{\rho}}^H$ , resulting in a lower radial stiffness, according to (13).

Algorithm 1 exits after 28 iterations, yielding the layout,  $\tau_{\text{D2,E}}$ , the adapted mesh and the repeated pattern in the bottom row of Fig. 5, from left to right, respectively. The new design is perfectly X-shaped, correcting the asymmetry shown in the top row. The corresponding mechanical properties are provided by

$$E_{\tau_{\text{D2,E}}}^H = \begin{pmatrix} 1.709 & 1.617 & 0.002 \\ 1.617 & 1.560 & 0.000 \\ 0.002 & 0.000 & 0.991 \end{pmatrix}, \quad \mathcal{M}_{\tau_{\text{D2,E}}} = 0.119, \\ K_r^m = 0.030, \quad f^m = 0.946,$$

which demonstrate the capability of ATOMS to produce an enhanced version of  $Y_{\text{obs}}^{\text{D2}}$ , while satisfying all imposed constraints. Specifically, the radial force is markedly reduced, achieving a decrease of 62%, while the components of the stiffness tensor remain within the admissible range. Moreover, the foreshortening is only slightly affected by the prescriptions in the enhancement scenario, showing a 5% difference. Most importantly, the contact area is noticeably reduced with respect to the original layout, endowing the new design with a lower post-intervention risk.

From a computational perspective, the design of  $\tau_{\text{D2,E}}$  is supported by an adapted mesh that tunes shape, size and orientation along the material/void interface, while modifying only the size within the interior of the layout, resulting in a total of 11,752 elements. As observed in  $\tau_{\text{D2}}$ , the presence of straight diagonal struts emphasizes the anisotropy of the tessellation, which reaches a maximum value  $s_K^{\text{max}} = 997.36$ .

### 3.5 Design $\tau_{\text{EVFX}}$

The last test case is devoted to replicate and enhance the mechanical properties of the Everflex-based design. Unit cell  $Y_{\text{obs}}^{\text{EVFX}}$  is rectangular with an aspect ratio equal to 1.6. For this reason, we choose  $Y$  as the rectangular domain  $(0, 16) \times (0, 10)$ , discretized with an initial structured mesh,  $\mathcal{T}_h^{(0)}$ , composed of 18000 isotropic elements. To drive the ATOMS procedure, we assign the values for  $E_{1111,\text{obs}}^H$ ,  $E_{2222,\text{obs}}^H$ ,  $E_{1212,\text{obs}}^H$ ,  $E_{1122,\text{obs}}^H$  as those in the third row of (23).

**Consistency test** The consistency check is performed by setting  $\gamma = 0.25$ , allowing for a larger design space compared to the setting used in Sects. 3.3-3.4. This choice is carried out to assess the robustness of ATOMS with respect to parameter  $\gamma$  and to manage the more complex scenario associated with the Everflex, thus avoiding non-feasible sets of constraints. After 24 iterations, we obtain the result in the top row, left panel of Fig. 6, along with the matching adapted grid and the pattern repetition (center and right panel, respectively). The layout concentrates stiffness along the  $x_1$ -direction, featuring a substantial quasi-horizontal block of material, while keeping the vertical joints as light as possible. This observation is compliant with the characteristics of  $Y_{\text{obs}}^{\text{EVFX}}$  and is reflected in the homogenized stiffness tensor, the contact area, and the microscopic radial stiffness and foreshortening of  $\tau_{\text{EVFX}}$ , given by

$$E_{\tau_{\text{EVFX}}}^H = \begin{pmatrix} 6.858 & 0.546 & -0.002 \\ 0.546 & 0.081 & 0.000 \\ -0.002 & 0.000 & 0.383 \end{pmatrix}, \quad \mathcal{M}_{\tau_{\text{EVFX}}} = 0.178, \\ K_r^m = 0.038, \quad f^m = 0.080.$$

Although the high difference imposed between the stiffness tensor com-

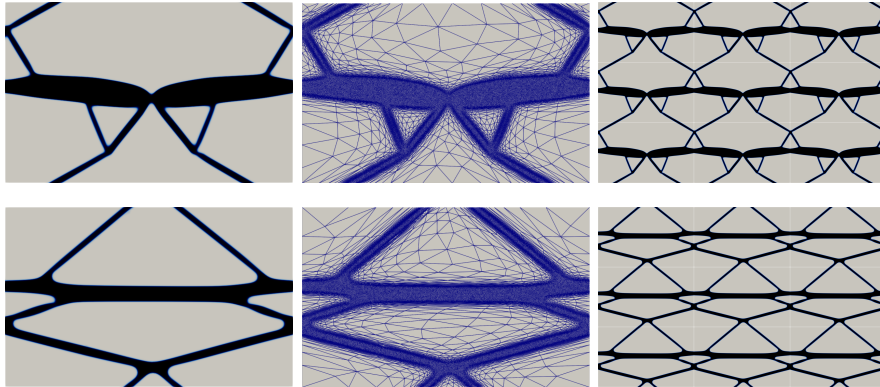


Figure 6: Design  $\tau_{\text{EVFX}}$ : consistency (top) and enhancement (bottom) test results in terms of optimized unit cell (left), adapted computational mesh (center), and  $3 \times 3$  planar periodic pattern (right).

ponents along the  $x_1$ - and  $x_2$ -direction is significant, the resulting values for  $E_{1111, \bar{\rho}}^H$  and  $E_{2222, \bar{\rho}}^H$  are fully compliant with the prescriptions. The foreshortening exactly matches the value for  $f^m$  (23), while the radial stiffness is larger. Regarding the mass fraction, the optimized design effectively lowers the contact area, consequently lowering the risk of adverse clinical complications. These favorable properties are achieved at a reasonable computational cost thanks to the use of an anisotropic adapted mesh. In particular, the final grid consists of 24236 triangles, with the most elongated elements ( $s_K^{\text{max}} = 956.32$ ) aligned with the directional features of the design.

**Enhancement test** Enhancing the Everflex commercial stent is a challenging objective. By noticing that the original design  $Y_{\text{obs}}^{\text{EVFX}}$  features a very low radial stiffness when compared with layouts  $Y_{\text{obs}}^{\text{D1}}$  and  $Y_{\text{obs}}^{\text{D2}}$  in (23), we challenge Algorithm 1 to design a new unit cell characterized by a larger value for  $K_r^m$ . For this purpose, we set  $\gamma = 0.20$  and we modify the constraint for  $E_{2222,\bar{\rho}}^H$  as

$$(1 + \gamma)E_{2222,\text{obs}}^H \leq E_{2222,\bar{\rho}}^H(\mathbf{u}^{*,22}, \mathbf{u}^{*,22}) \leq (1 + 2\gamma)E_{2222,\text{obs}}^H,$$

thus pushing the optimizer to reach a greater stiffness component along the  $x_2$ -direction. The resulting layout is reported in the bottom row, left panel of Fig. 6, where a main horizontal bar is vertically connected by means of two asymmetric polygons. The corresponding quantitative results, given by

$$E_{\tau_{\text{EVFX},E}}^H = \begin{pmatrix} 7.448 & 0.599 & -0.001 \\ 0.599 & 0.091 & 0.000 \\ -0.001 & 0.000 & 0.428 \end{pmatrix}, \quad \mathcal{M}_{\tau_{\text{EVFX},E}} = 0.173, \\ K_r^m = 0.043, \quad f^m = 0.080,$$

highlight the expected behavior, with a predominant stiffness component along the  $x_1$ -direction, a reduced value for the vertical one, and the prescribed orthotropic characteristics. Moreover, the contact area is reduced, in accordance with the minimization of the objective functional, the fore-shortening remains unchanged, while the radial stiffness is increased, aligning with the enhancement goal.

The mesh in the center panel further corroborates the strengths of the adaptive approach, by proposing a tessellation tailored to the evolving design at hand. This grid is composed of 24720 triangles with a maximum elongation given by 1012.01. Finally, the repetition of the pattern is shown in the right panel of Fig. 6.

## 4 Generation and testing of 3D stent virtual prototypes

To prepare the device for clinical use, a digital twin approach enables the precise generation and testing of 3D stent virtual prototypes. This framework allows the simulation of realistic physiological conditions, facilitating *in silico* iterations for optimizing the stent design, performance, and safety [35]. In the sequel, we describe the procedure adopted to generate the 3D virtual stent geometry. Then, we present the approach to evaluate the performance of the preliminary digital twin in response to the radial crimping mechanical test (see the third panel in Fig. 1).

### 4.1 From the 2D unit cell to the 3D stent device

3D models of vascular stents are generated from the 2D unit cells delivered by Algorithm 1 (see Fig. 7, panel (a) for an example of a stent virtual

prototype). The construction of the 3D stent model is implemented with Hypermesh software (Altair Engineering, Troy, MI, USA) and follows the procedure outlined in [33]. As a first step, the 2D layout is scaled to match the size of unit cells in existing devices. Next, the cell is projected onto a cylindrical surface with a 7 mm diameter, and then repeated 10 times circumferentially and 5 times axially. These repetitions minimize boundary effects in structural mechanics, aligning with standard values in literature for laser-cut stents. Finally, the surface lattice is extruded along the negative radial direction to achieve a constant strut thickness of 0.2 mm, typical for stents [67, 3, 16, 18, 19]. The chosen geometric characterization of the 3D stent model makes the values for  $r_H$  and  $S_{\min,2D}$  in Sect. 3.2 physically meaningful, here corresponding to the minimum strut size  $S_{\min,3D} = 50 \mu\text{m}$  in the physical domain, which meets standard requirements for laser-cutting technologies.

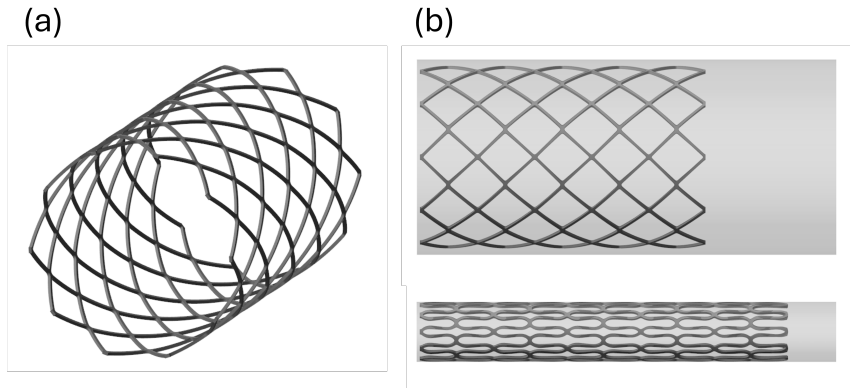


Figure 7: 3D stent geometry reconstruction through axial and radial repetitions (panel (a)), Crimping test: device at rest (top) and in crimped state (bottom) (panel (b)).

The generation of the 3D device from the 2D unit cell layout benefits from the modeling and computational advantages of operating on a 2D plane rather than on a 3D surface. In [36], it has been confirmed that this simplified approach, combined with the extrusion step to produce the 3D structure, does not compromise the reliability of the mechanical analysis compared to a fully 3D setting. In addition, this 2D-to-3D design paradigm is coherent with the laser-cutting manufacturing that assembles 2D components in 3D shapes, through techniques like bending, folding, or stacking.

Further good properties of ATOMS algorithm are inherited from the 3D virtual device generation, such as:

- Innovation: the enhancement tests prove that ATOMS allows us to push the limits of stent design towards more ambitious properties with

respect to the devices consolidated on the market. This good property has been already observed in other application contexts (see, e.g., [65]);

- **Automatization:** the user is relieved from an intensive parameter tuning during the design process. Parameters  $\text{tol}_\eta$  and  $h_{\text{iso}}$  are essentially the only values that need to be specified for Algorithm 1 to generate the final layout;
- **Limited post-processing:** the use of elongated elements in correspondence with the material/void interface (see Fig. 8, center panel) leads to the sharp detection of the structure boundaries. This feature avoids any smoothing post-processing operation when creating the 3D `.stl` file for mechanical analysis and manufacturing;
- **Manufacturability:** the use of adapted anisotropic meshes allows for the creation of structures with small minimum strut size, unattainable on uniform meshes with a similar cardinality. This capability helps meet stringent minimum length scale constraints in the actual 3D manufacturing process (see Fig. 8, right panel, where the circle diameter  $d = 0.376$  is compliant with the minimal strut size  $S_{\text{min},2D}$ );
- **Free-form:** the combination of SIMP with anisotropic mesh adaptation leads to out-of-the-box topologies, as shown, for instance, in [53, 55, 65, 57]. In the design of stents, this feature leads to the proposal of breakthrough devices when compared with those currently in use.

the optimized layout meets the manufacturability criteria more easily. In fact, the resolution of the computational mesh can affect the imposition of the minimum length scale, since a too coarse grid may lead to excessively thick structures. Conversely, the use of unstructured and adapted elements helps to meet manufacturability requirements (see Fig. 8, right panel, where the circle inscribed in the stent strut exceeds the imposed minimal size);

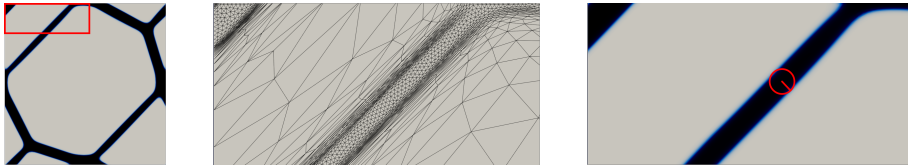


Figure 8: Post-processing and manufacturability for ATOMS - Design  $\tau_{D1}$ : optimized layout for the consistency test (left), corresponding zoom of the mesh (center) and of the density field where the circle associated with the strut size is red-highlighted.

## 4.2 Analysis of the virtual stent device through the crimping test

Consistently with the loading scenario in Sect. 2.1.2, we virtually perform a radial crimping at body temperature [33]. This setting mimics the loading conditions experienced by vascular stents when crimped to be inserted into a catheter, prior to deployment in the vessel [12, 13].

The mechanical analysis of the digital prototype is performed by exploiting a FE model implemented with Hypermesh (Altair Engineering, Troy, MI, USA) in conjunction with Abaqus/Explicit (Dassault Systèmes Simulia Corp., Johnston, RI, USA). The stent is discretized using C3D8R hexahedral elements with reduced integration, considering 8 and 10 elements across the strut width and thickness, respectively according to [33, 68]. The crimping catheter is modeled as a rigid cylindrical surface with a diameter of 7.5 mm and discretized using rigid surface elements (SFM3D4R) [69].

We remark that a nonlinear FE analysis is required to accurately capture the mechanical response of the stent during the crimping test although the optimized 2D unit cells are generated assuming linear elastic material behavior [33]. Indeed, nonlinearities have to be considered since the stent structure experiences high deformations, is prone to buckling, and the self-expandable stent constitutive material, NiTi, exhibits super-elasticity properties. The mechanical behavior of NiTi is described using the super-elastic constitutive model developed by F. Auricchio and R.L. Taylor [70], with material parameters derived from the computational study on self-expandable femoral stents in [71].

As initial condition, we apply a uniform temperature field of 37°C to all nodes of the stent. Thereafter, the crimping cylinder is compressed by applying a radial displacement to its nodes, which reduces the diameter from 7.5 mm to 2.3 mm (corresponding to a 7 Fr catheter), and the nodes on the left boundary are constrained in the axial direction (see Fig. 7 (b)). Contact between the stent and the crimping cylinder, and self-contacts between the stent struts are modeled by assuming a friction coefficient equal to 0.1 and a hard-contact pressure-overclosure relationship [33]. Furthermore, we ensure that the overall kinetic energy remains negligible when compared to the total internal strain energy, in order to conduct a quasi-static analysis [72].

Figure 9 illustrates the strain of the six devices tested virtually under radial crimping conditions at the minimum crimping diameter. It emerges that Design  $\tau_{D1}$ , in both the consistency and enhanced versions, as well as the consistency version of Design  $\tau_{EVFX}$ , fails to achieve full closure, as the peak value of the maximum principal strain exceeds the allowable limit of the material (NiTi elongation at break is assumed to be 18% [33]), as shown in Fig. 9 (a), (b), (e). In contrast, the consistency and enhanced versions of Design  $\tau_{D2}$ , as well as the enhanced version of Design  $\tau_{EVFX}$ , successfully close at the minimum crimping diameter without exhibiting material failure.

Specifically, the peak values of maximum principal strain at the minimum diameter remain below the material elongation limit at break, with values equal to 16%, 13%, and 12% for the two versions of Design  $\tau_{D2}$  and the enhanced layout of Design  $\tau_{EVFX}$ , respectively (see Fig. 9 (c), (d), (f)).

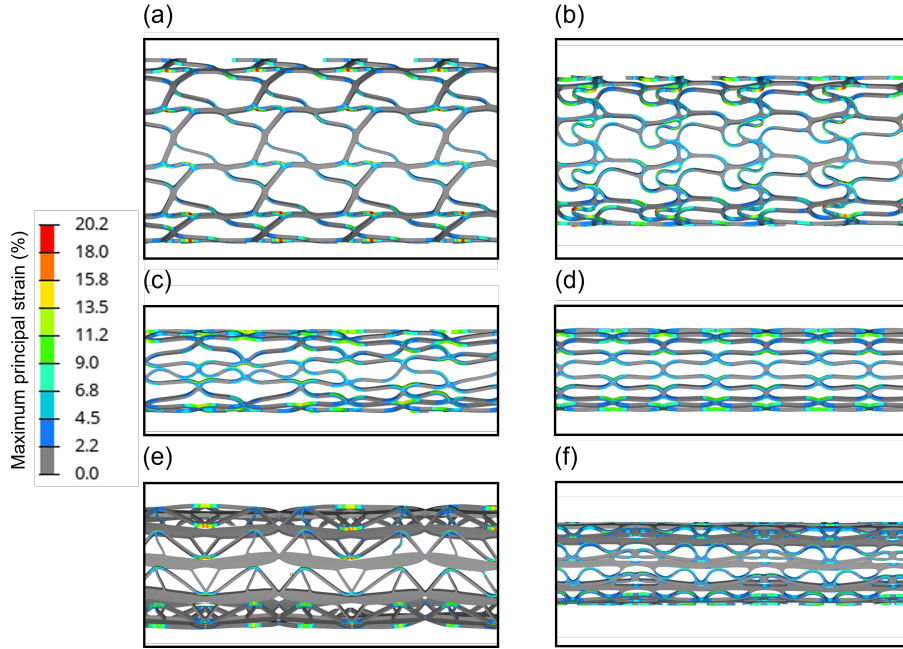


Figure 9: Analysis of the virtual stent device: contour plot of maximum principal strain under radial crimping conditions for the 3D virtual prototypes of Design  $\tau_{D1}$  (a)-(b), Design  $\tau_{D2}$  (c)-(d) and Design  $\tau_{EVFX}$  (e)-(f), for the consistency (left column) and the enhanced (right column) configuration. Half stent of each design is represented in section.

## 5 Conclusions

In this work, we proposed the ATOMS formulation to generate innovative vascular stent designs that replicate or improve the mechanical performance of existing devices used as a baseline. The mathematical formulation relies on a SIMP-based TO procedure enriched with homogenization theory to appropriately constrain the mechanical response of the designed stent, combined with a minimum length scale filtering scheme to ensure manufacturability.

The computational design framework is automated through the adoption of anisotropic adapted meshes. Specifically, integrating a TO formulation with a mesh adaptation procedure has proven crucial for delivering reliable results while minimizing computational costs. This approach facilitates the

seamless generation of a 3D virtual stent. In line with the concept of a digital twin [35], we virtually simulated the crimping of the stent into the catheter, mimicking the procedure typically performed to prepare the device for clinical use.

The numerical results demonstrated that the ATOMS framework is robust across various observed geometries characterized by different unit cell shapes and homogenized stiffness tensor components. Moreover, selecting the mass fraction (namely, the contact area between the device and the vessel) of the stent unit cell as the objective functional ensures that the final layouts are less prone to post-intervention complications. The radial crimping test conducted on the virtual prototypes allowed us to differentiate between the stent designs that cannot be successfully inserted into the catheter and the devices that can be virtually crimped without compromising material integrity.

The proposed procedure is a promising attempt in the creation of a computational platform for the analysis and enhancement of vascular stent designs. Its scope can be broadened, for instance, by implementing other *in silico* tests in a modular fashion, or by targeting other biomedical applications. Moreover, we aim at employing reduced order modeling techniques for the *in silico* test campaigns, to ensure a real-time response of the device to various mechanical stimuli, thus granting ATOMS the potential of functioning as a comprehensive digital twin.

## Acknowledgments

This study was carried out within the project “RESET: Rethinking femoral artery Stents for the trEatment of lower-limb peripheral arTery disease”, funded by the European Union – NextGenerationEU, Italian Ministry of University and Research, Italy, within the PRIN 2022 PNRR program (D.D. 1409 del 14/09/2022). NF and SP acknowledge the support by MUR, grant Dipartimento di Eccellenza 2023–2027. NF, SP are members of the Gruppo Nazionale Calcolo Scientifico–Istituto Nazionale di Alta Matematica (GNCS–INdAM). NF acknowledges the INdAM–GNCS 2024 Project “Accuratezza geometrica e adattività di griglia per problemi con interfacce complesse”. FM acknowledges the support of the research fund FAR 2023 DIP - Fondo di Ateneo per la Ricerca per il finanziamento di progetti di ricerca dipartimentali (Department of Engineering “Enzo Ferrari”, University of Modena and Reggio Emilia) and participates to the GNCS project MOMENTI - MOdelli e METodi Numerici per il Trattamento delle Immagini (Gruppo Nazionale per il Calcolo Scientifico - Istituto Nazionale di Alta Matematica “Francesco Severi”).

## References

- [1] M. Hejazi, F. Sassani, J. Gagnon, Y. Hsiang, A. S. Phani, Deformation mechanics of self-expanding venous stents: Modelling and experiments, *J. Biomech.* 120 (2021) 110333.
- [2] W. Jiang, W. Zhao, T. Zhou, L. Wang, T. Qiu, A Review on manufacturing and post-processing technology of vascular stents, *Micromachines* 13 (1) (2022) 140.
- [3] C. Pan, Y. Han, J. Lu, Structural design of vascular stents: A review, *Micromachines* 12 (7) (2021) 770.
- [4] B. Polanec, J. Kramberger, S. Glodež, A review of production technologies and materials for manufacturing of cardiovascular stents, *Adv. Prod. Eng. Manag.* 15 (4) (2020) 390–402.
- [5] E. Shlofmitz, M. Iantorno, R. Waksman, Restenosis of drug-eluting stents: A new classification system based on disease mechanism to guide treatment and state-of-the-art review, *Circ. Cardiovasc. Interv.* 12 (8) (2019) e007023.
- [6] A. K. Kareem, M. M. Gabir, I. R. Ali, A. E. Ismail, I. Taib, N. Darlis, O. M. Almoayed, A review on femoropopliteal arterial deformation during daily lives and nickel-titanium stent properties, *J. Med. Eng. Technol.* 46 (4) (2022) 300–317.
- [7] A. Qiao, Z. Zhang, Numerical simulation of vertebral artery stenosis treated with different stents, *J. Biomech. Eng.* 136 (4) (2014) 041007.
- [8] R. A. Byrne, M. Joner, A. Kastrati, Stent thrombosis and restenosis: What have we learned and where are we going? the Andreas Grüntzig Lecture ESC 2014, *Eur. Heart J.* 36 (47) (2015) 3320–3331.
- [9] R. Reejhsinghani, A. S. Lotfi, Prevention of stent thrombosis: Challenges and solutions, *Vasc. Health Risk Manag.* 11 (2015) 93–106.
- [10] K. C. Koskinas, Y. S. Chatzizisis, A. P. Antoniadis, G. D. Giannoglou, Role of endothelial shear stress in stent restenosis and thrombosis: Pathophysiologic mechanisms and implications for clinical translation, *J. Am. College Cardiol.* 59 (15) (2012) 1337–1349.
- [11] D. Károly, M. Kovács, A. A. Terdik, E. Bognár, Investigation of metallic surface area of coronary stents, *Biomechanica Hungarica* 6 (2013).
- [12] ISO, Cardiovascular implants — Endovascular devices — Part 2: Vascular stents (2012).

- [13] FDA, Non-clinical engineering tests and recommended labeling for intravascular stents and associated delivery systems (2010).
- [14] G. Alaimo, F. Auricchio, M. Conti, M. Zingales, Multi-objective optimization of nitinol stent design, *Med. Eng. Phys.* 47 (2017) 13–24.
- [15] R. Clune, D. Kelliher, J. C. Robinson, J. S. Campbell, NURBS modeling and structural shape optimization of cardiovascular stents, *Struct. Multidiscip. Optim.* 50 (1) (2014) 159–168.
- [16] E. Masoumi Khalil Abad, D. Pasini, R. Cecere, Shape optimization of stress concentration-free lattice for self-expandable Nitinol stent-grafts, *J. Biomech.* 45 (6) (2012) 1028–1035.
- [17] S. Pant, G. Limbert, N. P. Curzen, N. W. Bressloff, Multiobjective design optimisation of coronary stents, *Biomaterials* 32 (31) (2011) 7755–7773.
- [18] S. Pant, N. W. Bressloff, G. Limbert, Geometry parameterization and multidisciplinary constrained optimization of coronary stents, *Biomech. Model. Mechanobiol.* 11 (1-2) (2012) 61–82.
- [19] N. S. Ribeiro, J. Folgado, H. C. Rodrigues, Surrogate-based multi-objective design optimization of a coronary stent: Altering geometry toward improved biomechanical performance, *Int. J. for Numer. Methods Biomed. Eng.* 37 (6) (2021) e3453.
- [20] W. Wu, L. Petrini, D. Gastaldi, T. Villa, M. Vedani, E. Lesma, B. Previtali, F. Migliavacca, Finite element shape optimization for biodegradable magnesium alloy stents, *Ann. Biomed. Eng.* 38 (9) (2010) 2829–2840.
- [21] M. M. Torki, S. Hassanajili, M. M. Jalisi, Design optimizations of PLA stent structure by FEM and investigating its function in a simulated plaque artery, *Math. Comput. Simul.* 169 (2020) 103–116.
- [22] S. Čanić, L. Grubišić, D. Lacmanović, M. Ljulj, J. Tambača, Optimal design of vascular stents using a network of 1D slender curved rods, *Comput. Methods Appl. Mech. Engrg.* 394 (2022) 114853.
- [23] D. Carbonaro, A. Lucchetti, A. L. Audenino, T. Gries, T. J. Vaughan, C. Chiastra, Multi-objective design optimization of bioresorbable braided stents, *Comput. Methods Programs Biomed.* 242 (2023) 107781.

- [24] D. Carbonaro, S. Zambon, A. Corti, D. Gallo, U. Morbiducci, A. L. Audenino, C. Chiastra, Impact of nickel–titanium super-elastic material properties on the mechanical performance of self-expandable transcatheter aortic valves, *J. Mech. Behavior Biomed. Mater.* 138 (2023) 105623.
- [25] A. Kapoor, N. Jepson, N. Bressloff, P. Loh, T. Ray, S. Beier, The road to the ideal stent: A review of stent design optimisation methods, findings, and opportunities, *Mater. Des.* 237 (2024) 112556.
- [26] D. Carbonaro, D. Gallo, U. Morbiducci, A. Audenino, C. Chiastra, In silico biomechanical design of the metal frame of transcatheter aortic valves: multi-objective shape and cross-sectional size optimization, *Struct. Multidiscip. Optim.* 64 (4) (2021) 1825–1842.
- [27] J. B. Russ, R. L. Li, A. R. Herschman, H. Waisman, V. Vedula, J. W. Kysar, D. Kalfa, Design optimization of a cardiovascular stent with application to a balloon expandable prosthetic heart valve, *Mater. Des.* 209 (2021) 109977.
- [28] L. Meng, W. Zhang, L. Tang, J. Zhu, T. Gao, From topology optimization design to additive manufacturing: Today’s success and tomorrow’s roadmap, *Arch. Comput. Methods Eng.* 27 (2020) 805–830.
- [29] W. Wu, D. Z. Yang, Y. Y. Huang, M. Qi, W. Q. Wang, Topology optimization of a novel stent platform with drug reservoirs, *Med. Eng. Phys.* 30 (9) (2008) 1177–1185.
- [30] K. A. James, H. Waisman, Layout design of a bi-stable cardiovascular stent using topology optimization, *Comput. Methods Appl. Mech. Engrg.* 305 (2016) 869–890.
- [31] H. Xue, Z. Luo, T. Brown, S. Beier, Design of self-expanding auxetic stents using topology optimization, *Front. Bioeng. Biotechnol.* 8 (2020) 736.
- [32] H. Xue, S. C. Saha, S. Beier, N. Jepson, Z. Luo, Topological optimization of auxetic coronary stents considering hemodynamics, *Front. Bioeng. Biotechnol.* 9 (2021) 728914.
- [33] D. Carbonaro, F. Mezzadri, N. Ferro, G. De Nisco, A. L. Audenino, D. Gallo, C. Chiastra, U. Morbiducci, S. Perotto, Design of innovative self-expandable femoral stents using inverse homogenization topology optimization, *Comput. Methods Appl. Mech. Engrg.* 416 (2023) 116288.
- [34] H. X. Li, W. L. Shi, Z. Tan, M. J. Wang, D. Y. Zhao, J. Yan, Topology optimization for polymeric stent, *Struct. Multidiscip. Optim.* 65 (7) (2022) 194.

- [35] M. Viceconti, M. D. Vos, S. Mellone, L. Geris, Position paper from the digital twins in healthcare to the virtual human twin: A moon-shot project for digital health research, *IEEE J. Biomed. Health Inform.* 28 (1) (2024) 491–501.
- [36] D. Carbonaro, N. Ferro, F. Mezzadri, D. Gallo, A. Audenino, S. Perotto, U. Morbiducci, C. Chiastra, Easy-to-use formulations based on the homogenization theory for vascular stent design and mechanical characterization, *Comput. Methods Programs Biomed.* 257 (2024) 108467.
- [37] A. Bensoussan, J. L. Lions, G. Papanicolaou, *Asymptotic Analysis for Periodic Structures*, AMS Chelsea Publishing, Providence, RI, 2011.
- [38] O. Sigmund, *Design of material structures using topology optimization*, Ph.D. thesis, Technical University of Denmark, Lyngby, Denmark (1994).
- [39] J. M. Guedes, N. Kikuchi, Preprocessing and postprocessing for materials based on the homogenization methods with adaptive finite element methods, *Comput. Methods Appl. Mech. Engrg.* 83 (1990) 143–198.
- [40] G. Qi, C. X. Liu, K. Feng, L. Ma, K. U. Schröder, Analytical solutions of stress distribution within a hollow cylinder under contact interactions, *Int. J. Mech. Sci.* 239 (2023) 107897.
- [41] F. P. Beer, R. Johnston, J. Dewolf, D. Mazurek, *Mechanics of Materials*, McGraw-Hill, 2013.
- [42] M. S. Cabrera, C. W. Oomens, F. P. Baaijens, Understanding the requirements of self-expandable stents for heart valve replacement: Radial force, hoop force and equilibrium, *J. Mech. Behavior Biomed. Mater.* 68 (2017) 252–264.
- [43] O. Sigmund, K. Maute, Topology optimization approaches: A comparative review, *Struct. Multidiscip. Optim.* 48 (2013) 1031–1055.
- [44] G. Allaire, F. Jouve, A.-M. Toader, Structural optimization using sensitivity analysis and a level-set method, *J. Comput. Phys.* 194 (1) (2004) 363–393.
- [45] M. P. Bendsøe, O. Sigmund, *Topology Optimization: Theory, Methods and Applications*, 2nd Edition, Springer, 2004.
- [46] N. Ferro, S. Micheletti, S. Perotto, Density-based inverse homogenization with anisotropically adapted elements, in: A. Corsini, S. Perotto, G. Rozza, H. van Brummelen (Eds.), *Numerical Methods for Flows*, vol 132. *Lecture Notes in Computational Science and Engineering.*, Springer, 2020, pp. 211–221.

- [47] B. S. Lazarov, F. Wang, O. Sigmund, Length scale and manufacturability in density-based topology optimization, *Arch. Appl. Mech.* 86 (1) (2016) 189–218.
- [48] F. Wang, B. S. Lazarov, O. Sigmund, On projection methods, convergence and robust formulations in topology optimization, *Struct. Multidisc. Optim.* 43 (2011) 767–784.
- [49] B. S. Lazarov, O. Sigmund, Filters in topology optimization based on Helmholtz-type differential equations, *Int. J. Numer. Methods Eng.* 86 (6) (2011) 765–781.
- [50] K. Svanberg, The method of moving asymptotes—a new method for structural optimization, *Int. J. Numer. Methods Eng.* 24 (2) (1987) 359–373.
- [51] A. Wächter, L. T. Biegler, On the implementation of an interior-point filter line-search algorithm for large-scale nonlinear programming, *Math. Program.* 1, Ser. A (106) (2006) 25–57.
- [52] O. Sigmund, J. Petersson, Numerical instabilities in topology optimization: a survey on procedures dealing with checkerboards, mesh-dependencies and local minima, *Struct. Multidisc. Optim.* 16 (1) (1998) 68–75.
- [53] S. Micheletti, S. Perotto, L. Soli, Topology optimization driven by anisotropic mesh adaptation: towards a free-form design, *Comput. Struct.* 214 (2019) 60 – 72.
- [54] N. Ferro, S. Micheletti, S. Perotto, An optimization algorithm for automatic structural design, *Comput. Methods Appl. Mech. Engrg.* 372 (2020) 113335.
- [55] D. Cortellessa, N. Ferro, S. Perotto, S. Micheletti, Enhancing level set-based topology optimization with anisotropic graded meshes, *Appl. Math. Comput.* 447 (2023) 127903.
- [56] S.-W. Cheng, T. K. Dey, J. R. Shewchuk, *Delaunay mesh generation*, Chapman & Hall/CRC Computer and Information Science Series, Chapman & Hall/CRC, Boca Raton, FL, 2013.
- [57] M. Gavazzoni, N. Ferro, S. Perotto, S. Foletti, Multi-physics inverse homogenization for the design of innovative cellular materials: Application to thermo-elastic problems, *Math. Comput. Appl.* 27 (1) (2022) 15.
- [58] N. Ferro, S. Perotto, M. Gavazzoni, A new fluid-based strategy for the connection of non-matching lattice materials, *Struct. Multidisc. Optim.* 65 (10) (2022) 287, 15.

- [59] D. di Cristofaro, C. Galimberti, D. Bianchi, R. Ferrante, N. Ferro, M. Mannisi, S. Perotto, Adaptive topology optimization for innovative 3D printed metamaterials, in: Proceedings of WCCM-ECCOMAS 2020 Conference - Modeling and Analysis of Real World and Industry Applications, Vol. 1200, 2021.
- [60] S. Micheletti, S. Perotto, Anisotropic adaptation via a Zienkiewicz-Zhu error estimator for 2D elliptic problems, in: G. Kreiss, P. Lötstedt, A. Målqvist, M. Neytcheva (Eds.), Numerical Mathematics and Advanced Applications, Springer-Verlag Berlin Heidelberg, 2010, pp. 645–653.
- [61] O. C. Zienkiewicz, J. Z. Zhu, A simple error estimator and adaptive procedure for practical engineering analysis, *Int. J. Numer. Methods Eng.* 24 (2) (1987) 337–357.
- [62] O. C. Zienkiewicz, J. Z. Zhu, The superconvergent patch recovery and a posteriori error estimates. Part I. The recovery technique, *Int. J. Numer. Methods Eng.* 33 (7) (1992) 1331–1364.
- [63] L. Formaggia, S. Perotto, New anisotropic a priori error estimates, *Numer. Math.* 89 (4) (2001) 641–667.
- [64] S. Micheletti, S. Perotto, Reliability and efficiency of an anisotropic Zienkiewicz-Zhu error estimator, *Comput. Methods Appl. Mech. Engrg.* 195 (9-12) (2006) 799–835.
- [65] N. Ferro, S. Perotto, D. Bianchi, R. Ferrante, M. Mannisi, Design of cellular materials for multiscale topology optimization: application to patient-specific orthopedic devices, *Struct. Multidiscip. Optim.* 65 (3) (2022) 79.
- [66] F. Hecht, BAMG: Bidimensional anisotropic mesh generator, <https://www.ljll.math.upmc.fr/hecht/ftp/bamg/bamg.pdf> (2006).
- [67] M. Colombo, A. Corti, D. Gallo, A. Colombo, G. Antognoli, M. Bernini, C. McKenna, S. Berceci, T. Vaughan, F. Migliavacca, C. Chiastra, Superficial femoral artery stenting: Impact of stent design and overlapping on the local hemodynamics, *Comput. Biol. Med.* 144 (2022) 105248.
- [68] C. Chiastra, M. J. Grundeken, C. Collet, W. Wu, J. J. Wykrzykowska, G. Pennati, G. Dubini, F. Migliavacca, Biomechanical impact of wrong positioning of a dedicated stent for coronary bifurcations: A virtual bench testing study, *Cardiovasc. Eng. Technol.* 9 (3) (2018) 415–426.
- [69] D. Carbonaro, C. Chiastra, U. Morbiducci, A. Audenino, Transcatheter aortic valve with embolic filter: Experiments and simulations, in: *Convegno Nazionale di Bioingegneria*, 2020, pp. 457–460.

- [70] F. Auricchio, R. L. Taylor, Shape-memory alloys: modelling and numerical simulations of the superelastic behavior, *Comput. Methods Appl. Mech. Engrg.* 143 (3-4) (1997) 175–194.
- [71] C. Gökgöl, N. Diehm, F. R. Nezami, P. Büchler, Nitinol Stent Oversizing in Patients Undergoing Popliteal Artery Revascularization: A Finite Element Study, *Ann. Biomed. Eng.* 43 (12) (2015) 2868–2880.
- [72] D. Carbonaro, E. Villa, D. Gallo, U. Morbiducci, A. L. Audenino, C. Chiastra, Designing the mechanical behavior of NiTi self-expandable vascular stents by tuning the heat treatment parameters, *J. Mech. Behav. Biomed. Mater.* 158 (2024) 106653.

## MOX Technical Reports, last issues

Dipartimento di Matematica  
Politecnico di Milano, Via Bonardi 9 - 20133 Milano (Italy)

- 96/2024** Brivio, S.; Fresca, S.; Manzoni, A.  
*PTPI-DL-ROMs: Pre-trained physics-informed deep learning-based reduced order models for nonlinear parametrized PDEs*
- 93/2024** Conti, P.; Kneifl, J.; Manzoni, A.; Frangi, A.; Fehr, J.; Brunton, S.L.; Kutz, J.N.  
*VENI, VINDy, VICI - a variational reduced-order modeling framework with uncertainty quantification*
- 94/2024** Franco, N.R.; Fresca, S.; Tombari, F.; Manzoni, A.  
*Deep Learning-based surrogate models for parametrized PDEs: handling geometric variability through graph neural networks*
- 95/2024** Zacchei, F.; Rizzini, F.; Gattere, G.; Frangi, A.; Manzoni, A.  
*Neural networks based surrogate modeling for efficient uncertainty quantification and calibration of MEMS accelerometers*
- 91/2024** Ciaramella, G.; Kartmann, M.; Mueller, G.  
*Solving Semi-Linear Elliptic Optimal Control Problems with L1-Cost via Regularization and RAS-Preconditioned Newton Methods*
- 86/2024** Franco, N.R.; Fraulin, D.; Manzoni, A.; Zunino, P.  
*On the latent dimension of deep autoencoders for reduced order modeling of PDEs parametrized by random fields*
- Castiglionea, C.; Arnonec, E.; Bernardi, M.; Farcomeni, A.; Sangalli, L.M.  
*PDE-regularised spatial quantile regression*
- 88/2024** Regazzoni, F.; Poggesi, C.; Ferrantini, C.  
*Elucidating the cellular determinants of the end-systolic pressure-volume relationship of the heart via computational modelling*
- 85/2024** Brivio, S.; Franco, Nicola R.; Fresca, S.; Manzoni, A.  
*Error estimates for POD-DL-ROMs: a deep learning framework for reduced order modeling of nonlinear parametrized PDEs enhanced by proper orthogonal decomposition*
- 90/2024** Tomasetto, M.; Arnone, E.; Sangalli, L.M.  
*Modeling anisotropy and non-stationarity through physics-informed spatial regression*